



Originally published as:

Schulze, K., Marquardt, H., Kawazoe, T., Boffa Ballaran, T., McCammon, C., Koch-Müller, M., Kurnosov, A., Marquardt, K. (2018): Seismically invisible water in Earth's transition zone? - *Earth and Planetary Science Letters*, 498, pp. 9—16.

DOI: <http://doi.org/10.1016/j.epsl.2018.06.021>

Seismically invisible water in Earth's transition zone?

Kirsten Schulze^{1,§}, Hauke Marquardt^{1,2}, Takaaki Kawazoe³, Tiziana Boffa Ballaran¹, Catherine McCammon¹, Monika Koch-Müller⁴, Alexander Kurnosov¹, Katharina Marquardt¹

¹ Bayerisches Geoinstitut BGI, University of Bayreuth, 95440 Bayreuth, Germany

² Department of Earth Sciences, University of Oxford, OX1 3AN Oxford, UK

³ Department of Earth and Planetary Systems Sciences, Hiroshima University, 739-8526 Higashi-Hiroshima, Japan

⁴ German Research Center for Geosciences GFZ, 14473 Potsdam, Germany

a b s t r a c t

Ringwoodite, the dominant mineral at depths between 520 km and 660 km, can store up to 2–3 wt. % of water in its crystal structure, making the Earth's transition zone a plausible water reservoir that plays a central role in Earth's deep water cycle. Experiments show that hydration of ringwoodite significantly reduces elastic wave velocities at room pressure, but the effect of pressure remains poorly constrained. Here, a novel experimental setup enables a direct quantification of the effect of hydration on ringwoodite single-crystal elasticity and density at pressures of the Earth's transition zone and high temperatures. Our data show that the hydration-induced reduction of seismic velocities almost vanishes at conditions of the transition zone. Seismic data thus agree with a wide range of water contents in the transition zone.

1. Introduction

The Earth's transition zone extends between depths of 410 km and 660 km and could host a water reservoir that has been stable over geological timescales, thereby playing a key role in the dynamic and geochemical evolution of the entire mantle (Bercovici and Karato, 2003). A hydrous transition zone might be associated with local melting events that are detectable above (Song et al., 2004) and below the transition zone (Schmandt et al., 2014) and may even be the source region for continental flood basalts (Wang et al., 2015), affecting the global climate and possibly contributing to mass extinction events throughout Earth's history.

The hypothesis of the transition zone being a deep water reservoir is based on high-pressure high-temperature experiments showing that the nominally anhydrous minerals (Mg,Fe)₂SiO₄ wadsleyite and ringwoodite, constituting up to 60 vol.% of transition zone rocks (Frost, 2008), can incorporate significant amounts of hydrogen ("water") as point defects into their crystal structures (Kohlstedt et al., 1996). The recent discovery of a hydrous ringwoodite inclusion in a natural diamond containing about 1.5 wt.%

of water (Pearson et al., 2014) confirms experimental predictions and strengthens the hypothesis of a (at least partly) hydrated transition zone. However, this single observation does not constrain the global amount of water stored in the transition zone or its spatial distribution. Instead, global scale three-dimensional mapping of the water content in the transition zone requires geophysical remote sensing.

Previous experimental and theoretical studies have reported a significant reduction of elastic wave velocities with hydration for Mg₂SiO₄ ringwoodite (Inoue et al., 1998; Wang et al., 2003) as well as iron-bearing ringwoodite (Jacobsen et al., 2004) at ambient pressure. More limited experimental work indicates that this effect prevails to high pressures (Wang et al., 2006) and high temperatures (Mao et al., 2012), suggesting that reduced seismic wave velocities in the transition zone can be employed to map mantle hydration (Wang et al., 2006; Mao et al., 2012).

However, significant extrapolation of previous high-pressure experiments is required to quantify effects of hydration at transition zone pressures for ringwoodite, leading to contradictory conclusions (Fig. 1). In addition, the effect of temperature on the high-pressure elasticity of hydrous ringwoodite is mostly unconstrained. The only available measurement of the elastic wave velocities of hydrous iron-bearing ringwoodite at pressures up to 16 GPa and temperatures of up to 670 K suggests that tempera-

§ E-mail address of the corresponding author:
Kirsten.Schulze(at)uni-bayreuth.de (K. Schulze).

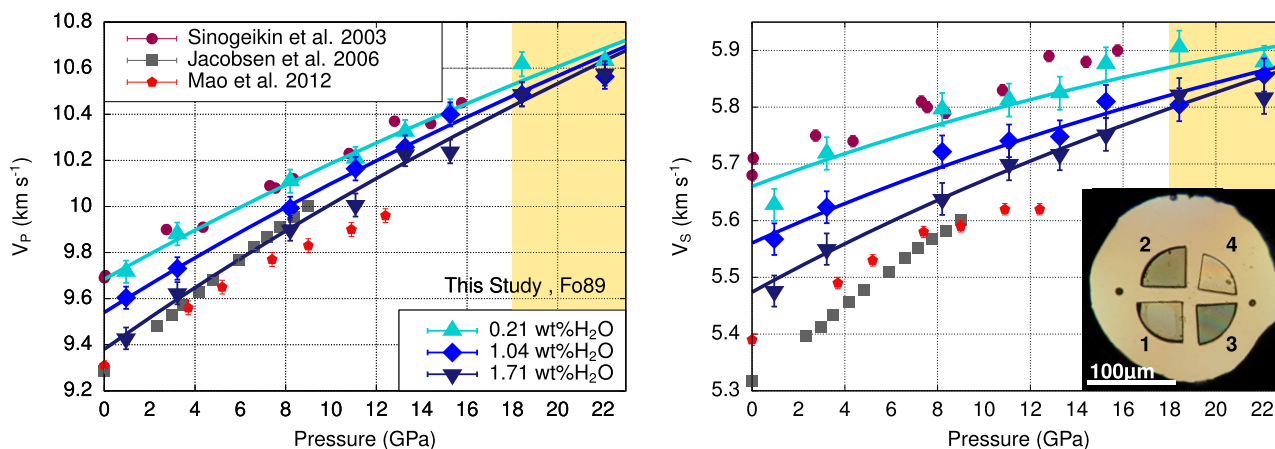


Fig. 1. Measured high-pressure acoustic wave velocities of $(\text{Mg}_{0.89}\text{Fe}_{0.11})_2\text{SiO}_4$ ringwoodite in comparison to previously published work (Mao et al., 2012; Jacobsen and Smyth, 2006; Sinogeikin et al., 2003). The inset shows our experimental setup where we simultaneously measured three single-crystal samples of Fe-bearing ringwoodite and one Mg-ringwoodite to high pressures. Samples 1–3: Fe-bearing ringwoodites with 0.21(3), 1.04(11) and 1.71(18) wt.% H_2O . Sample 4: Mg_2SiO_4 ringwoodite with 0.42(5) wt.% H_2O (Table 4 in supplementary material).

ture may strongly enhance the hydration-induced velocity reduction for compressional wave velocities (Mao et al., 2012). However, the effects of a temperature increase to 670 K on the elastic wave velocities are comparably small ($\sim 1\text{--}2\%$ reduction), while uncertainties in pressure and temperature determination are large in resistively-heated diamond-anvil cell work. This combination results in significant uncertainties when comparing the results to high-pressure/-temperature experiments on anhydrous ringwoodite that suffer from the same uncertainties.

In order to reliably quantify the effect of hydration on the seismic wave velocities of ringwoodite at transition zone pressures and elevated temperatures, we designed a novel type of experiment, taking advantage of recent methodological developments (Marquardt and Marquardt, 2012; Kurnosov et al., 2017; Schulze et al., 2017). In our experiment, four focused ion beam (FIB) cut single-crystal samples of three hydrated $(\text{Mg}_{0.89}\text{Fe}_{0.11})_2\text{SiO}_4$ ringwoodite (Fo89) as well as one sample of Mg-ringwoodite (Fo100) were loaded together in the pressure chamber of a diamond-anvil cell (Fig. 1).

2. Material and methods

2.1. Sample synthesis and characterisation

San Carlos olivine was used as a starting material for synthesising the iron-containing ringwoodites. In two cases liquid water was added to synthesise hydrated samples. The Mg-endmember ringwoodite was grown from pure forsterite powder with no water added. The multi-anvil experimental conditions ranged between 19–22 GPa and 1200–1600 °C (Table 3 in supplementary material). The run products contained single crystals of ringwoodite with sizes on the order of 100 μm . For the iron-containing samples an increase in crystal size, structural quality and deepness of blue colour is observed with increasing water content. The Mg-endmember is colourless.

The hydration state of all samples was determined by unpolarized Fourier transform infrared spectroscopy (FTIR). FTIR was favoured over secondary ion mass spectroscopy (SIMS) as it allowed for measuring the hydration state of the double-side polished samples which were later loaded in the DAC. Depending on the platelet size, three to seven equally distributed FTIR spectra were taken for each platelet. All spectra were normalized and fringe (Neri et al., 1987) and background corrected. The integrated area and the position of the main peak between 2500 and 4000 cm^{-1} was calculated using a Voigt peak function. The

molar absorption coefficient was calculated from the calibration of Thomas et al. (2015) and the molar concentration using the Lambert–Beer law. All samples were measured on the same instrument and were processed identically. This procedure ensures a maximum degree of comparability among the samples. An uncertainty of 10% in derived water content is considered reasonable for all samples due to uncertainties in sample thickness, the peak-fitted integrated areas and the absorption coefficient (Thomas et al., 2015). For the conversion to the more commonly used unit of wt.% H_2O , the density at ambient conditions derived from the chemical analysis and x-ray diffraction was used. For the Fo89 composition water contents of 0.21(3) wt.%, 1.04(11) wt.% and 1.71(18) wt.% were determined for H4071, H4164 and H4166, respectively, as well as 0.42(5) wt.% for the Mg-endmember MA389.

To determine the oxidation state of the iron in the samples H4071, H4164 and H4166, both Mössbauer spectroscopy and electron energy loss spectroscopy (EELS) were performed at Bayerisches Geoinstitut (BGI) (Table 4, supplementary material). EELS was performed on the three iron-containing samples, but due to oxidation of the samples during measurement and despite considerable effort, only three evaluable spectra each could be acquired for H4071 and H4166. For all measurements high energy loss spectra and, for calibration, low energy loss spectra were acquired in a range of 670 to 772.35 eV and -10 to 92.35 eV, respectively. For each measurement an area on the sample was chosen manually and 50 frames were stacked to enhance spectrum quality, where the total exposure times were 250 s and 100 s for H4071 and H4166, respectively. The results for the ferric to total iron ratio $\text{Fe}^{3+}/\sum\text{Fe}$ range between 0.15 to 0.19 for H4071 and 0.10 to 0.15 for H4166.

Mössbauer spectroscopy was performed on samples extracted from high-pressure runs (either single crystal or polycrystalline aggregate) over regions of 500 μm diameter as previously described (McCammon et al., 2004). $\text{Fe}^{3+}/\sum\text{Fe}$ was determined from relative areas and uncertainties were assessed based on the results for different fitting models. The Mössbauer spectroscopy results are in good agreement with the results from EELS and are also in agreement with earlier studies (McCammon et al., 2004), considering both the absolute values and the absence of any correlation between hydration state and Fe^{3+} concentrations (Table 4 in supplementary material).

Electron microprobe analysis (EMPA) was performed on the three iron-bearing samples to determine the chemical composition. The Mg-endmember was synthesised from Mg_2SiO_4 and is

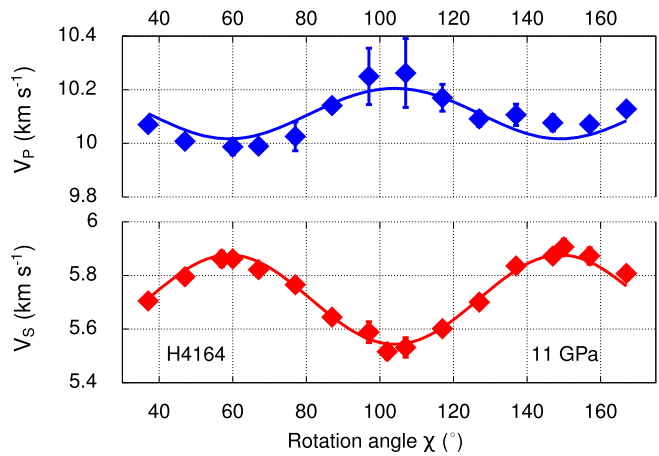
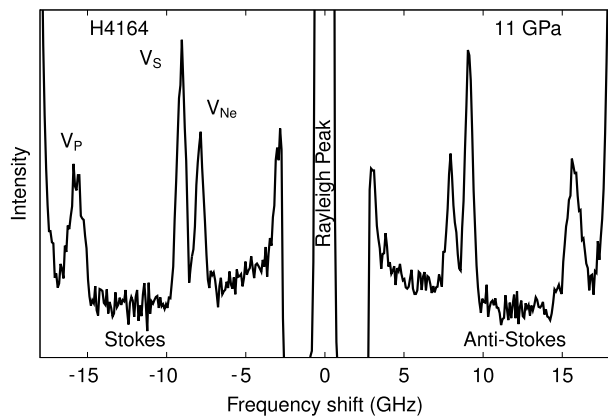


Fig. 2. A typical Brillouin spectroscopy spectrum collected at high pressure, displaying the symmetric Stokes and Anti-Stokes peaks of the longitudinal and shear velocities of the sample and one peak of the pressure transmitting medium (Ne). Right: The measured velocity anisotropy curve of the same sample at a pressure of 11 GPa along with the Christoffel fit (solid curves).

considered to be pure. The electron microprobe analysis was conducted at BGI on a JEOL Superprobe JXA-8200 WD/ED combined Micro-analyzer. The amounts of silicon, magnesium, iron, nickel, manganese, aluminium and calcium were measured using the following standards: olivine (Mg, Fe, Si), wollastonite (Ca), spinel (Al), MnTiO₃ (Mn) and metallic nickel (Ni). Any element besides iron, magnesium and silicon is only present in trace amounts or is under the detection limit. From each multi-anvil synthesis several crystals were fixed in Crystalbond™, polished and 12 nm carbon coated. Summed over all crystals ~300 individual points were measured for each run-product. The results from Mössbauer spectroscopy were used to correct the mass percentage amount of FeO for Fe³⁺. To derive the number of cations per formula unit, the molar ratios were normalised to four oxygens and the FTIR data were used to calculate the abundance of hydrogen atoms.

2.2. Brillouin spectroscopy and X-ray diffraction measurements

We conducted simultaneous measurements of sound wave velocity using Brillouin spectroscopy and density by X-ray diffraction at different pressures up to 22.1 GPa. Brillouin spectroscopy measurements were performed at DESY Hamburg (HP) and at BGI Bayreuth (HP/HT). The Brillouin spectroscopy system at DESY is operated in a forward scattering symmetry with a scattering angle of 50° at a laser wavelength of 532 nm. For signal detection a multi-pass tandem Fabry–Perot interferometer was used with either an avalanche photomultiplier or photodiode detector. The diamond-anvil cell which contains the samples is placed on a four circle Eulerian cradle which enables very fine adjustments of the cell within the laser beam. To measure the elastic anisotropy of the samples the cell is rotated about its compressional axis. In all samples the probed plane is {100} where the signal repeats after a 90° planar rotation. For the first pressure point at 0.97 GPa 11 measurements were performed, covering a 90° rotation angle in ten 10° step increments plus measurements at the angles where velocities show extreme values, which were calculated from preceding XRD measurements. Collection time for each spectrum was 3–10 h. For the remaining pressure points 14–18 orientations in a 130° range were measured, again with a 10° stepsize (Fig. 2). The frequency shifts measured by the interferometer can directly be translated to velocities using the laser wavelength and the scattering angle (Speziale et al., 2014). Velocities of a single-crystal of MgO were measured in a <100> direction at ambient conditions before and after every Brillouin spectroscopy session to verify the system calibration. The density was calculated from the unit-cell volumes obtained from single-crystal X-ray diffraction performed

Table 1

Results from a combined third-order Eulerian strain fit to all elastic constants at high pressure (Stixrude and Lithgow-Bertelloni, 2005). Listed are the elastic constants C_{ij} and moduli K , G and their pressure derivatives at room pressure. Iron ratio is defined $Fo = Mg/(Mg + \sum Fe)$.

		H4071	H4164	H4166	MA389
Fo	[-]	88.5(6)	88.8(8)	89.4(6)	100
c_{H_2O}	[mol L ⁻¹]	0.44(5)	2.10(21)	3.40(34)	0.83(9)
c_{H_2O}	[wt.%]	0.21(3)	1.04(11)	1.71(18)	0.42(5)
C_{11}^0	[GPa]	329.05(126)	314.71(62)	299.71(149)	324.96(186)
C'_{11}	[-]	6.30(11)	6.48(08)	6.97(13)	6.24(21)
C_{12}^0	[GPa]	118.34(151)	114.95(88)	109.96(180)	115.96(197)
C'_{12}	[-]	2.95(13)	3.14(11)	3.25(15)	2.69(23)
C_{44}^0	[GPa]	127.85(88)	122.22(50)	117.84(97)	129.87(145)
C'_{44}	[-]	0.92(05)	1.09(05)	1.19(08)	1.03(12)
K^0	[GPa]	188.57(109)	181.54(63)	173.21(130)	185.63(146)
K'^0	[-]	4.06(08)	4.25(10)	4.49(11)	3.87(17)
G^0	[GPa]	118.32(56)	112.73(31)	108.05(66)	119.05(86)
G'^0	[-]	1.59(5)	1.71(4)	1.89(6)	1.72(9)

before and after every Brillouin spectroscopy session. In each Brillouin spectrum the Rayleigh-peak and its ghosts as well as the peaks resulting from diamonds, one peak each of longitudinal and shear velocity from the sample and one or two peaks of the pressure medium (Ne) were fitted individually with Voigt peak functions. Overlapping peaks were deconvoluted with a doublet. From the frequency shifts we derived the velocities of the longitudinal and shear waves (Speziale et al., 2014). To derive the elastic constants we fit each pressure point to the Christoffel equation (Fig. 2, Table 5 in supplementary material). A third-order Eulerian finite strain equation (Stixrude and Lithgow-Bertelloni, 2005) was fitted to the elastic constants at high pressures to derive the elastic constants at room pressure and the corresponding pressure derivatives (Table 1). The Reuss and Voigt bounds of the elastic moduli were calculated from the elastic constants (Angel et al., 2009). Aggregate velocities are calculated as Reuss–Voigt–Hill averages.

The XRD measurements were performed on a single-crystal XRD system at BGI using a four circle goniometer, a MoK α rotating anode X-ray source focused using multilayer optics and a point detector (Angel et al., 1997). For each crystal 4–5 reflections were centred in 8-positions following the routine of King and Finger (1979) which is implemented in the SINGLE operating software (Angel and Finger, 2011) to determine the orientation matrix and the unit-cell parameters. Results for unit cell volume and density for all samples are shown in Fig. 3.

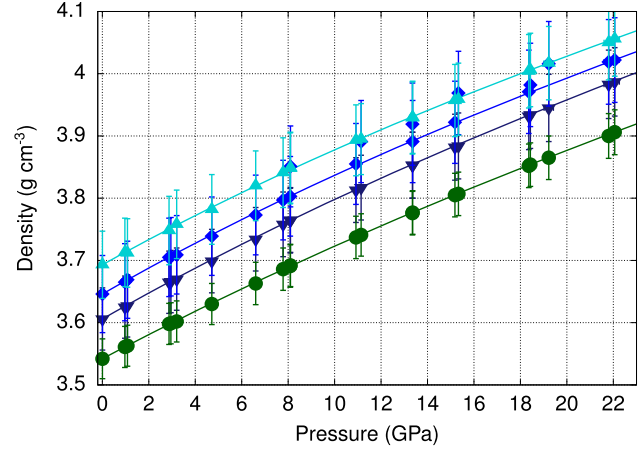
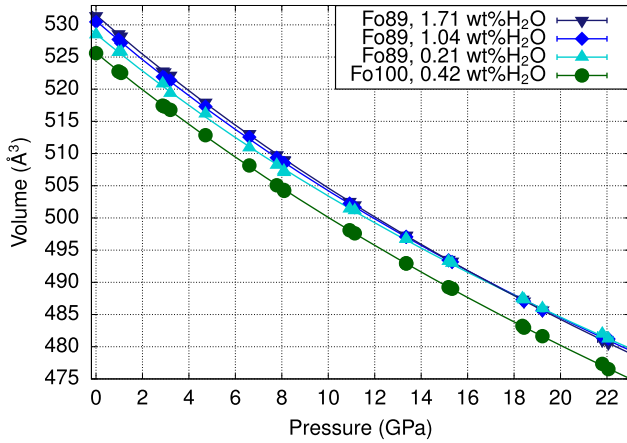


Fig. 3. Unit cell volumes and densities up to 22 GPa for the here studied ringwoodite samples. Unit-cell volumes were measured by single-crystal XRD. The unit-cell volumes of the Fo89 ringwoodites converge at transition zone pressures. This effect cannot be observed in the densities due to the dominant role of the pressure-independent mass.

2.3. Simultaneous high-pressure and high-temperature measurements

In addition to the high-pressure measurements, we performed a high-temperature measurement at pressures of the Earth's transition zone. The simultaneous measurement of all samples ensures identical pressure and temperature conditions thereby improving data precision and eliminating a significant group of experimental uncertainties (Schulze et al., 2017). The high-pressure and -temperature measurements were performed on the combined XRD and Brillouin spectroscopy system at BGI. The system is operated with a laser wavelength of 532 nm, a scattering angle of 80° , and a multi-pass tandem Fabry-Perot interferometer with a photodiode detector. The collection time per spectrum was between 30 min and 3 h. The DAC was equipped with a resistive heater made up by a platinum wire coiled around a ceramic ring and placed around the pressure chamber. For initial temperature estimation a K-type thermocouple was placed as close as possible to the pressure chamber. During heating the cell was flushed with argon creating an oxygen depleted atmosphere to prevent the diamonds and gasket from oxidising. The unit-cell volumes of the samples were measured at high-pressure and -temperature with the above described XRD system. Due to the additional cables from the heater and thermocouple and the argon tube the range of the χ -cradle was limited to $\pm 90^\circ$. This limits the procedure to 4-position centring, which was performed on 4–5 reflections for each crystal. The exact pressure and temperature conditions were derived by cross-correlating the unit-cell volumes measured by XRD and the shift of the ruby fluorescence line from in situ Raman spectroscopy. Data published in Katsura et al. (2004) were used to correct the unit-cell volume for thermal expansion and the calibrations given in Dewaele et al. (2008) and Rekhii et al. (1999) were employed for pressure and temperature corrections of the ruby shift.

3. Results and discussion

3.1. Dependence of the sound wave velocities of Fo89 ringwoodite on hydration state and pressure

We observe a clear reduction of all room pressure elastic constants with increasing hydration state for our three Fe-bearing ringwoodite samples (Fig. 1, Table 1), qualitatively consistent with earlier observations (Inoue et al., 1998; Mao et al., 2012; Jacobsen and Smyth, 2006). When increasing the amount of incorporated water from 0.21 wt.% to 1.71 wt.%, the bulk and shear moduli decrease from 188.6(11) GPa and 118.3(6) GPa to 173.2(13) GPa

and 108.1(7) GPa, respectively. In contrast, the pressure derivatives of the elastic constants systematically increase with hydration state (Table 1), leading to a marked suppression of the hydration effect on elastic wave velocities at high pressure (Fig. 4). In a first approximation, the elastic constants, moduli and the aggregate velocities can be considered to be linearly dependent on the hydration state, $c_{\text{H}_2\text{O}}$, at a given pressure. For the three Fo89 compositions the hydration dependency of both aggregate velocities V_P and V_S were fitted with a linear equation for each pressure point individually (Fig. 4). The pressure dependence of the slope was approximated to be linear, resulting in the equations:

$$V_P(P, c_{\text{H}_2\text{O}}) = (0.00310(24) \cdot P - 0.0956(17)) \cdot c_{\text{H}_2\text{O}} + V_P(P, 0) \quad (1)$$

$$V_S(P, c_{\text{H}_2\text{O}}) = (0.00178(17) \cdot P - 0.0615(14)) \cdot c_{\text{H}_2\text{O}} + V_S(P, 0). \quad (2)$$

The pressure P is given in GPa and the hydration state $c_{\text{H}_2\text{O}}$ in molL^{-1} . The velocities are in units of km s^{-1} . At pressures corresponding to the stability field of ringwoodite in Earth's transition zone, the average velocities of our iron-bearing samples are identical within their respective error bars (Figs. 1 and 4). Our direct observation thus contradicts previous assumptions about the significant effect of hydration on seismic wave velocities that have been widely employed in the interpretation of seismic observations (Houser, 2016; Suetsugu et al., 2006; Meier et al., 2009).

3.2. Comparison of the hydration effect between Fo89 and Fo100 ringwoodite

Comparison of our measurements on Mg_2SiO_4 ringwoodite with previous data (Wang et al., 2006) confirms the observed trend for our Fe-bearing samples (Fig. 5). Applying equations (1) and (2) to the function fitted to the data of our study to account for the differences in hydration state results in good agreement with the data from the literature. We conclude that the hydration dependencies are applicable to ringwoodite with both Fo89 and Fo100 compositions. Further support comes from previous computational work at 0 K that reported a possible velocity crossover with pressure between hydrous and anhydrous Mg-ringwoodite for certain water incorporation mechanisms (Li et al., 2009). Our velocity-based findings are further supported by our X-ray diffraction measurements that show a decreasing effect of hydration on the unit cell volume with pressure (Fig. 3).

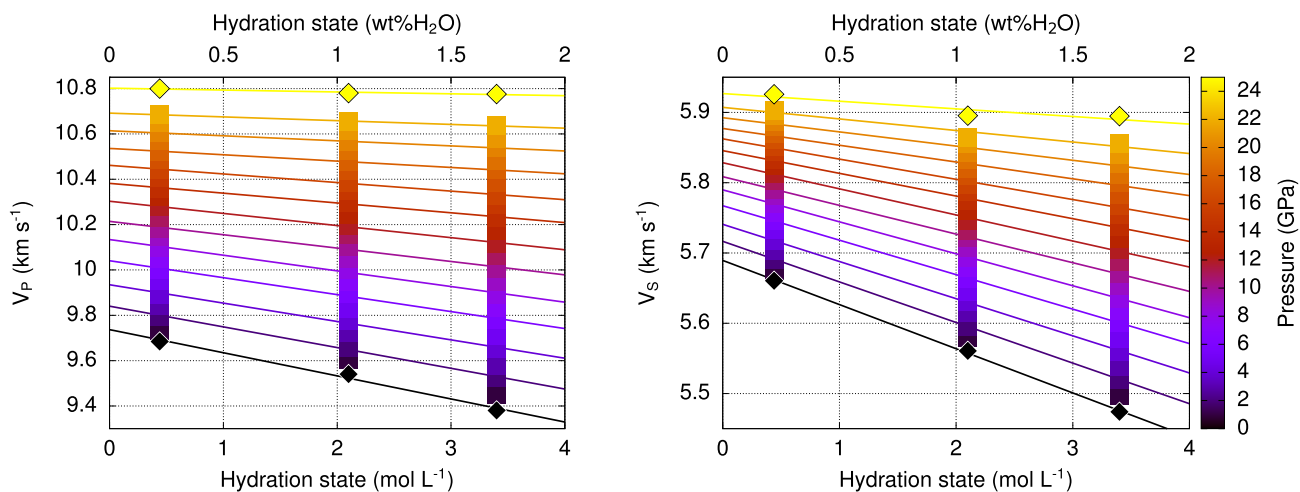


Fig. 4. Dependency of elastic wave velocities of $(\text{Mg}_{0.89}\text{Fe}_{0.11})_2\text{SiO}_4$ ringwoodite on hydration state determined from our high-pressure measurements using the multi-sample approach. Experimental data points have been interpolated (squares) and extrapolated (diamonds) based on a finite strain formalism. A linear decrease of velocities with hydration is assumed. (For interpretation of the colours in the figure(s), the reader is referred to the web version of this article.)

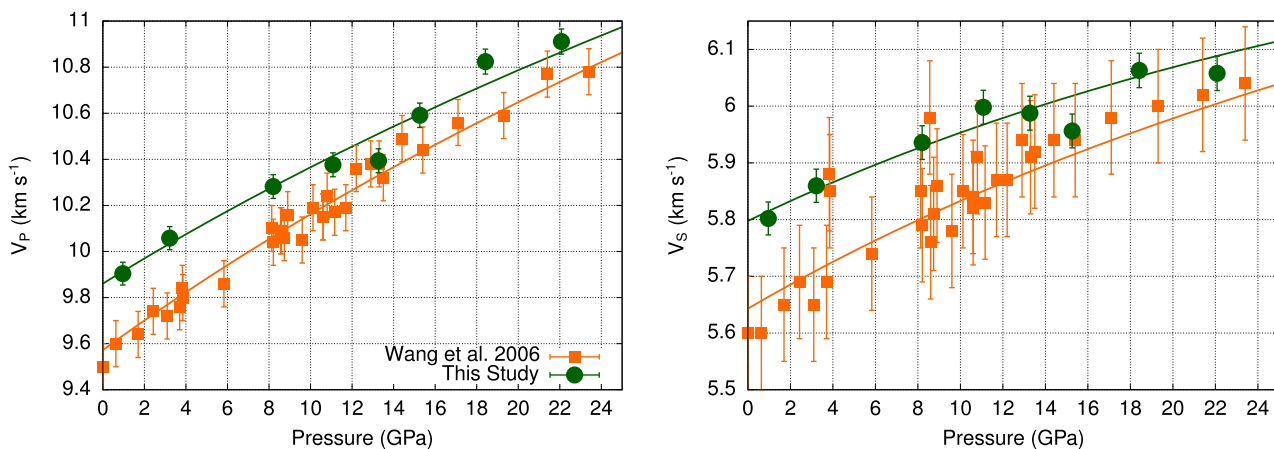


Fig. 5. The longitudinal and shear aggregate velocities of the Mg-endmember ringwoodite MA389 from this study and the hydrated sample of Wang et al. (2006). Comparison of the datasets show a convergence at transition zone pressures similar to what is observed in Fo89 ringwoodite. The curve through the data of Wang et al. (2006) is calculated using the finite strain equation parameters that we derived for our Mg-endmember sample (Table 2) plus a correction for the difference in hydration state from equations (1) and (2).

3.3. Simultaneous high-pressure and high-temperature measurements

An additional experiment at simultaneous high-pressure and high-temperature was performed on all four ringwoodite samples at 19.9(5) GPa at a temperature of 500(20) K (Table 2). We find the effect of temperature on the velocities of our ringwoodite samples to be independent of the hydration state within uncertainties. All our measured data are well described by the temperature dependency measured by an earlier work on anhydrous ringwoodite at ambient conditions (Sinogeikin et al., 2003) (Fig. 6). Our data thus indicate that the temperature effect at 500(20) K on ringwoodite wave velocities at 19.9(5) GPa is independent of the hydration state. We note, however, that the limited temperature stability of hydrous ringwoodite precludes experiments at high enough temperatures to reach any conclusive result about the effect of realistic mantle temperature on elastic properties at high pressure, particularly as non-linear effects have been reported in anhydrous ringwoodite at temperatures higher than 1200 K (Higo et al., 2008). We note that temperature might increase the sensitivity of elastic wave velocities to hydration through anelastic effects, but a quantitative estimate is severely hampered by the lack of any experimental constraints. According to earlier estimates based on parameters derived for olivine, this effect might lead to a velocity reduction of about 0.5 vel.% for ringwoodite hydrated with 1 wt.% of H_2O (Suetsugu et al., 2006).

Table 2

Results for Brillouin spectroscopy at 500(20) K and 19.9(4) GPa. Iron ratio is defined $\text{Fo} = \text{Mg}/(\text{Mg} + \sum\text{Fe})$.

		H4071	H4164	H4166	MA389
Fo	[-]	88.5(6)	88.8(8)	89.4(6)	100
$\text{c}_{\text{H}_2\text{O}}$	[mol L ⁻¹]	0.44(5)	2.10(21)	3.40(34)	0.83(9)
$\text{c}_{\text{H}_2\text{O}}$	[wt.%]	0.21(3)	1.04(11)	1.71(18)	0.42(5)
ρ	[g cm ⁻³]	4.00(6)	3.97(7)	3.96(6)	3.85(4)
C_{11}	[GPa]	436.7(15)	429.5(10)	422.6(17)	434.0(18)
C_{12}	[GPa]	166.8(16)	166.8(12)	167.7(24)	159.4(21)
C_{44}	[GPa]	140.5(10)	142.2(7)	136.0(15)	147.1(14)
G_R	[GPa]	138.2(10)	138.0(7)	132.5(13)	136.2(17)
G_V	[GPa]	138.3(8)	138.2(6)	132.6(11)	136.3(12)
K_S	[GPa]	256.8(12)	254.4(9)	252.7(17)	255.4(22)
V_P	[km s ⁻¹]	10.55(6)	10.47(6)	10.42(6)	10.66(6)
V_S	[km s ⁻¹]	5.90(3)	5.88(3)	5.79(3)	5.95(3)

3.4. Velocity reduction in a pyrolitic mantle with hydration and possible dependence on the hydrogen incorporation mechanisms

Based on our measurements, we modelled the effects of hydration on seismic wave velocities in a pyrolitic mantle as a function of pressure and ringwoodite hydration state (Fig. 7). At conditions expected in the transition zone, moderate amounts of water incor-

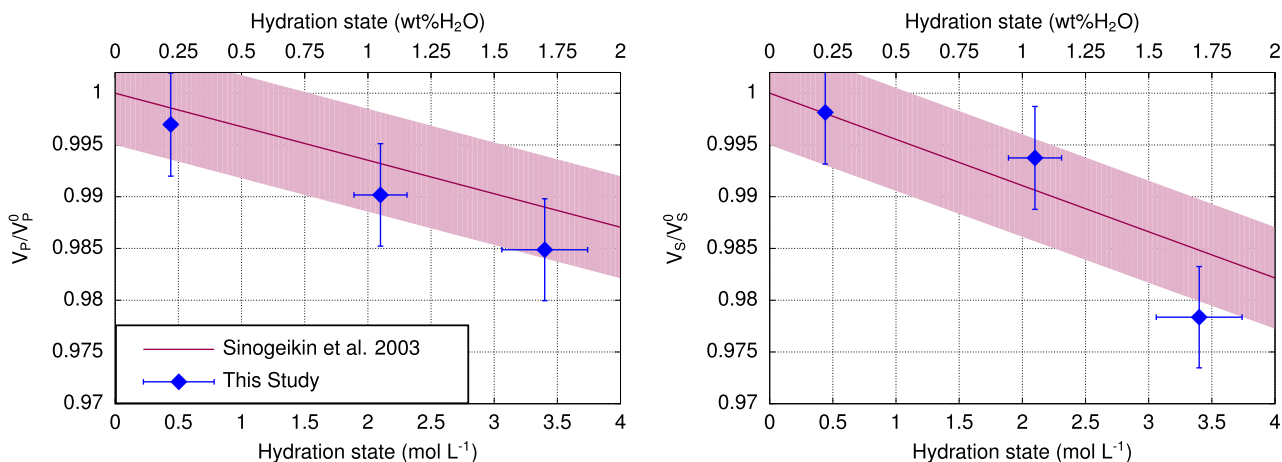


Fig. 6. Hydration dependency of wave velocities measured at transition zone pressures of 19.9(5) GPa and a temperature of 500(20) K (diamonds). The red solid line is a prediction based on applying a linear temperature dependency derived previously for anhydrous Fe-bearing ringwoodite at room pressure (Sinogeikin et al., 2003) to our 300 K high-pressure experimental data. Within uncertainties, our measured data are consistent with this prediction, indicating that the temperature-effect on wave velocities might be independent of hydration state.

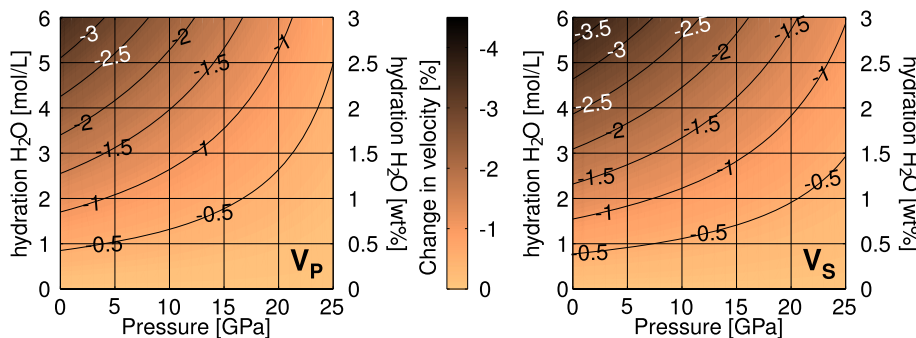


Fig. 7. Pressure-dependent velocity reduction expected in a pyrolytic mantle as a function of ringwoodite hydration. At pressures of the transition zone where ringwoodite is the stable phase (~ 18 – 25 GPa), the velocity reduction caused by 1 wt.% hydration is less than 0.5%. A similar behaviour is expected at mantle temperatures if temperature does not change the relative behaviour of anhydrous and hydrous ringwoodite, a hypothesis supported by our comparative high-temperature experiment (Fig. 6, see text).

porated into ringwoodite would almost certainly be hard to identify in seismic observables. Hydration of ringwoodite with 0.5 wt.% of water, for example, would decrease compressional and shear wave velocities by less than about 0.25 vel.%, possibly below the detection limit of seismic tomography (de Wit et al., 2012). Even if ringwoodite was almost water-saturated and contained 1.5 wt.% of water in the transition as found in a natural diamond inclusion (Pearson et al., 2014), seismic wave velocities would only be reduced by about 0.5 vel.%, where seismic shear velocities appear to be slightly more sensitive to hydration than compressional velocities (Fig. 7). Overall, our data reveal that hydration of ringwoodite only has a subtle effect on seismic velocities at conditions of the transition zone. This suggests that only strongly hydrated mantle regions might possibly be detectable by analyzing seismic wave speed variations, provided that they span over large enough lateral regions to produce a coherent seismic signal. Given the here-found small effect of hydration on ringwoodite wave velocities, the seismic detection of mantle hydration will likely be significantly complicated by competing effects of lateral temperature variations. A difference in temperature of 100 K would, for example, reduce the aggregate velocities by about 0.5 vel.% (Sinogeikin et al., 2003; Jackson et al., 2000). The results of our comparative study are in marked disagreement with the results of Mao et al. (2012) that predicted velocity reductions of 4.5 vel.% for shear and 7 vel.% for compressional wave velocities per wt.% H_2O in iron-bearing ringwoodite at pressure and temperature conditions of the lower transition zone.

Even though part of this discrepancy can be explained by uncertainties in extrapolating the previous data to pressures of the transition zone, we note that our low pressure measurements show a significantly smaller effect of hydration on elastic wave velocities than that inferred from the previous Brillouin spectroscopy work on iron-bearing ringwoodite containing 1.1 wt.% H_2O (Mao et al., 2012) (Fig. 1). This difference might result from different water-incorporation mechanisms between the studied ringwoodite samples. Previous studies have identified the three following major hydration mechanisms for ringwoodite (Li et al., 2009; Panero, 2010):

- (1) $\text{Mg}_{\text{Si}}'' + \text{H}^{*}$; (2) $V_{\text{Si}}''' + \text{H}^{****}$; (3) $V_{\text{Mg}}'' + \text{H}^{**}$

By comparison of measured unit cell volumes of our samples to the theoretically predicted volume dependence for specific hydration mechanisms, we infer that our samples closely resemble the energetically favoured ringwoodite defect structure expected in the transition zone (Panero, 2010) where hydrogen is mostly incorporated through mechanism (3) (Fig. 8). In contrast, the larger unit cell volume reported for the hydrous ringwoodite studied previously by Brillouin spectroscopy (Mao et al., 2012) might indicate a different dominant hydrogen substitution mechanism, possibly as a result of differences in the synthesis procedure. Theoretical work predicts a significant dependence of the expected velocity reduction on the water-incorporation mechanism for Mg-endmember ringwoodite, where incorporation mechanism (1) is expected to have the strongest effect (Panero, 2010), consistent with the intuition that a larger increase in unit cell volume causes a more pronounced effect on bulk elasticity (Fig. 3). Comparison of our

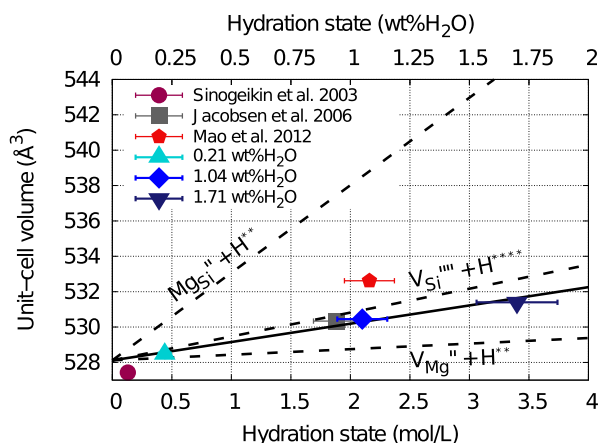


Fig. 8. Dependence of unit-cell volume on hydration predicted by computations for Mg_2SiO_4 ringwoodite (Panero, 2010). The dashed lines represent different isolated hydrogen substitution mechanism, whereas the solid line corresponds to the trend predicted for energetically-favoured hydration of ringwoodite, where hydration defect ratios are calculated to be 64:25:10 for substitution mechanisms (1):(2):(3) (Panero, 2010). These ratios are in good agreement with experimental results from nuclear resonance spectroscopy (Grüniger et al., 2017). The theoretically-derived unit cell volumes have been linearly shifted in volume to match the volume for an-hydrous Fe-bearing ringwoodite determined in this study. Our measured unit-cell volumes for hydrated Fe-bearing ringwoodite (diamonds) closely follow the pre-dicted trend. Literature unit-cell volumes are reported for comparison (Mao et al., 2012; Jacobsen and Smyth, 2006; Sinogeikin et al., 2003).

study to the previous work (Mao et al., 2012) suggests that the same principles apply to iron-bearing ringwoodite.

4. Conclusion

Based on our comparative velocity measurements on typical transition zone ringwoodite and our recent work on wadsleyite (Buchen et al., 2018), we conclude that water might not be detectable by seismic wave speed variations in Earth's transition zone. Our findings provide an intuitive explanation for discrepancies in previous attempts to map the water distribution using seismic data, that concluded that the transition zone is strongly hydrated (Suetsugu et al., 2006), dry (Houser, 2016), or partly hydrated away from subducting slabs (Meier et al., 2009), conflicting with the assumption that slabs transport water into the mantle (Thompson, 1992). Our data can further explain discrepancies in inferred water contents from electrical conductivity studies and seismic tomography (Houser, 2016; Kelbert et al., 2009), for example under eastern China, where electrical conductivity values are strongly elevated, indicating significant hydration (Kelbert et al., 2009), but seismic wave velocities are not markedly lowered (Houser, 2016) as would be expected from previous results (Mao et al., 2012). Based on our findings, the seismic record is also consistent with a much wider range of water contents in the transition zone than inferred by previous studies and seismological constraints accord with a locally (Pearson et al., 2014) or even globally (Fei et al., 2017) water-saturated transition zone.

Acknowledgements

This research was supported through the project "GeoMaX" funded under the Emmy-Noether Program of the German Science Foundation DFG [MA4534/3-1]. HM acknowledges support from the Bavarian Academy of Sciences. We thank S. Speziale for assistance using the Brillouin spectroscopy system at DESY Hamburg. The Brillouin scattering system hosted at the Extreme Conditions Infrastructure laser lab (PETRA III) is run by the Deutsches GFZ in collaboration with DESY. The FEI Scios focused ion beam machine

at BGI Bayreuth is supported by the German Science Foundation [INST 91/315-1 FUGG].

Appendix A. Supplementary material

Supplementary material related to this article can be found online at <https://doi.org/10.1016/j.epsl.2018.06.021>.

References

- Angel, R.J., Finger, L.W., 2011. SINGLE: a program to control single-crystal diffractometers. *J. Appl. Crystallogr.* 44 (1), 247–251.
- Angel, R.J., Allan, D.R., Miletich, R., Finger, L.W., 1997. The use of quartz as an internal pressure standard in high-pressure crystallography. *J. Appl. Crystallogr.* 30 (4), 461–466. <https://doi.org/10.1107/S0021889897000861>.
- Angel, R.J., Jackson, J.M., Reichmann, H., Speziale, S., 2009. Elasticity measurements on minerals: a review. *Eur. J. Mineral.* 21, 525–550.
- Bercovici, D., Karato, S.-i., 2003. Whole-mantle convection and the transition-zone water filter. *Nature* 425 (6953), 39. <https://doi.org/10.1038/nature01918>.
- Buchen, J., et al., 2018. High-pressure single-crystal elasticity of wadsleyite and the seismic signature of water in the shallow transition zone. *Earth Planet. Sci. Lett.* <https://doi.org/10.1016/j.epsl.2018.06.027>. In press.
- de Wit, R.W.L., Trampert, J., van der Hilst, R.D., 2012. Toward quantifying uncertainty in travel time tomography using the null-space shuttle. *J. Geophys. Res., Solid Earth* 117, B03301. <https://doi.org/10.1029/2011JB008754>.
- Dewaele, A., Torrent, M., Loubeyre, P., Mezouar, M., 2008. Compression curves of transition metals in the Mbar range: experiments and projector augmented-wave calculations. *Phys. Rev. B* 78 (10), 104102. <https://doi.org/10.1103/PhysRevB.78.104102>.
- Fei, H., Yamazaki, D., Sakurai, M., Miyajima, N., Ohfujii, H., Katsura, T., Yamamoto, T., 2017. A nearly water-saturated mantle transition zone inferred from mineral viscosity. *Sci. Adv.* 3 (6), e1603024. <https://doi.org/10.1126/sciadv.1603024>.
- Frost, D.J., 2008. The upper mantle and transition zone. *Elements* 4 (3), 171–176. <https://doi.org/10.2113/GSELEMENTS.4.3.171>.
- Grüniger, H., Armstrong, K., Greim, D., Boffa-Ballaran, T., Frost, D.J., Senker, J., 2017. Hidden oceans? Unraveling the structure of hydrous defects in the Earth's deep interior. *J. Am. Chem. Soc.* 139 (30), 10499–10505. <https://doi.org/10.1021/jacs.7b05432>.
- Higo, Y., Inoue, T., Irifune, T., Funakoshi, K.-i., Li, B., 2008. Elastic wave velocities of $(\text{Mg}_{0.91}\text{Fe}_{0.09})_2\text{SiO}_4$ ringwoodite under P–T conditions of the mantle transition region. *Phys. Earth Planet. Inter.* 166 (3), 167–174. <https://doi.org/10.1016/j.pepi.2008.01.003>.
- Houser, C., 2016. Global seismic data reveal little water in the mantle transition zone. *Earth Planet. Sci. Lett.* 448, 94–101. <https://doi.org/10.1016/j.epsl.2016.04.018>.
- Inoue, T., Weidner, D.J., Northrup, P.A., Parise, J.B., 1998. Elastic properties of hydrous ringwoodite (γ -phase) in Mg_2SiO_4 . *Earth Planet. Sci. Lett.* 160 (1), 107–113. [https://doi.org/10.1016/S0012-821X\(98\)00077-6](https://doi.org/10.1016/S0012-821X(98)00077-6).
- Jackson, J.M., Sinogeikin, S.V., Bass, J.D., 2000. Sound velocities and elastic properties of γ - Mg_2SiO_4 to 873 K by Brillouin spectroscopy. *Am. Mineral.* 85 (2), 296–303.
- Jacobsen, S.D., Smyth, J.R., 2006. Effect of water on the sound velocities of ringwoodite in the transition zone. In: Jacobsen, S.D., Lee, S.V.D. (Eds.), *Earth's Deep Water Cycle*. American Geophysical Union, pp. 131–145.
- Jacobsen, S.D., Smyth, J.R., Spetzler, H., Holl, C.M., Frost, D.J., 2004. Sound velocities and elastic constants of iron-bearing hydrous ringwoodite. *Phys. Earth Planet. Inter.* 143–144, 47–56. <https://doi.org/10.1016/j.pepi.2003.07.019>.
- Katsura, T., Yokoshi, S., Song, M., Kawabe, K., Tsujimura, T., Kubo, A., Ito, E., Tange, Y., Tomioka, N., Saito, K., Nozawa, A., Funakoshi, K.-i., 2004. Thermal expansion of Mg_2SiO_4 ringwoodite at high pressures. *J. Geophys. Res.* 109 (B12), B12209. <https://doi.org/10.1029/2004JB003094>.
- Kelbert, A., Schultz, A., Egbert, G., 2009. Global electromagnetic induction constraints on transition-zone water content variations. *Nature* 460 (7258), 1003. <https://doi.org/10.1038/nature08257>.
- King, H.E., Finger, L.W., 1979. Diffracted beam crystal centering and its application to high-pressure crystallography. *J. Appl. Crystallogr.* 12 (4), 374–378. <https://doi.org/10.1107/S0021889879012723>.
- Kohlstedt, D.L., Keppler, H., Rubie, D.C., 1996. Solubility of water in the α , β and γ phases of $(\text{Mg,Fe})_2\text{SiO}_4$. *Contrib. Mineral. Petrol.* 123 (4), 345–357. <https://doi.org/10.1007/s004100050161>.
- Kurnosov, A., Marquardt, H., Frost, D.J., Ballaran, T.B., Ziberna, L., 2017. Evidence for a Fe^{3+} -rich pyrolytic lower mantle from (Al,Fe)-bearing bridgmanite elasticity data. *Nature* 543 (7646), 543. <https://doi.org/10.1038/nature21390>.
- Li, L., Brodholt, J., Alfé, D., 2009. Structure and elasticity of hydrous ringwoodite: a first principle investigation. *Phys. Earth Planet. Inter.* 177 (3), 103–115. <https://doi.org/10.1016/j.pepi.2009.07.007>.
- Mao, Z., Lin, J.-F., Jacobsen, S.D., Duffy, T.S., Chang, Y.-Y., Smyth, J.R., Frost, D.J., Hauri, E.H., Prakapenka, V.B., 2012. Sound velocities of hydrous ringwoodite to 16 GPa

- and 673 K. *Earth Planet. Sci. Lett.* 331–332, 112–119. <https://doi.org/10.1016/j.epsl.2012.03.001>.
- Marquardt, H., Marquardt, K., 2012. Focused ion beam preparation and characterization of single-crystal samples for high-pressure experiments in the diamond-anvil cell. *Am. Mineral.* 97 (2–3), 299–304. <https://doi.org/10.2138/am.2012.3911>.
- McCammon, C.A., Frost, D.J., Smyth, J.R., Laustsen, H.M.S., Kawamoto, T., Ross, N.L., van Aken, P.A., 2004. Oxidation state of iron in hydrous mantle phases: implications for subduction and mantle oxygen fugacity. *Phys. Earth Planet. Inter.* 143–144, 157–169. <https://doi.org/10.1016/j.pepi.2003.08.009>.
- Meier, U., Trampert, J., Curtis, A., 2009. Global variations of temperature and water content in the mantle transition zone from higher mode surface waves. *Earth Planet. Sci. Lett.* 282 (1), 91–101. <https://doi.org/10.1016/j.epsl.2009.03.004>.
- Neri, F., Saitta, G., Chiofalo, S., 1987. A simple procedure to remove the interference fringes from optical spectra. *J. Phys., E J. Sci. Instrum.* 20 (7), 894. <https://doi.org/10.1088/0022-3735/20/7/015>.
- Panero, W.R., 2010. First principles determination of the structure and elasticity of hydrous ringwoodite. *J. Geophys. Res.* 115 (B3), B03203. <https://doi.org/10.1029/2008JB006282>.
- Pearson, D.G., Brenker, F.E., Nestola, F., McNeill, J., Nasdala, L., Hutchison, M.T., Matveev, S., Mather, K., Silversmit, G., Schmitz, S., Vekemans, B., Vincze, L., 2014. Hydrous mantle transition zone indicated by ringwoodite included within diamond. *Nature* 507 (7491), 221–224. <https://doi.org/10.1038/nature13080>.
- Rekhi, S., Dubrovinsky, L., Saxena, S., 1999. Temperature-induced ruby fluorescence shifts up to a pressure of 15 GPa in an externally heated diamond anvil cell. *High Temp.-High Pres.* 31 (3). <https://doi.org/10.1068/htrt161>.
- Schmandt, B., Jacobsen, S.D., Becker, T.W., Liu, Z., Dueker, K.C., 2014. Dehydration melting at the top of the lower mantle. *Science* 344 (6189), 1265–1268. <https://doi.org/10.1126/science.1253358>.
- Schulze, K., Buchen, J., Marquardt, K., Marquardt, H., 2017. Multi-sample loading technique for comparative physical property measurements in the diamond-anvil cell. *High Press. Res.* 37 (2), 159–169. <https://doi.org/10.1080/08957959.2017.1299719>.
- Sinogeikin, S.V., Bass, J.D., Katsura, T., 2003. Single-crystal elasticity of ringwoodite to high pressures and high temperatures: implications for 520 km seismic discontinuity. *Phys. Earth Planet. Inter.* 136 (1–2), 41–66.
- Song, T.-R.A., Helmberger, D.V., Grand, S.P., 2004. Low-velocity zone atop the 410-km seismic discontinuity in the northwestern united states. *Nature* 427 (6974), 530. <https://doi.org/10.1038/nature02231>.
- Speziale, S., Marquardt, H., Duffy, T.S., 2014. Brillouin scattering and its application in geosciences. *Rev. Mineral. Geochem.* 78 (1), 543–603. <https://doi.org/10.2138/rmg.2014.78.14>.
- Stixrude, L., Lithgow-Bertelloni, C., 2005. Thermodynamics of mantle minerals, 1: physical properties. *Geophys. J. Int.* 162, 610–632. <https://doi.org/10.1111/j.1365-246X.2005.02642.x>.
- Suetsugu, D., Inoue, T., Yamada, A., Zhao, D., Obayashi, M., 2006. Towards mapping the three-dimensional distribution of water in the transition zone from p-velocity tomography and 660-km discontinuity depths. In: Jacobsen, S.D., Lee, S.V.D. (Eds.), *Earth's Deep Water Cycle*. American Geophysical Union, pp. 237–249.
- Thomas, S.-M., Jacobsen, S.D., Bina, C.R., Reichart, P., Moser, M., Hauri, E.H., Koch-Müller, M., Smyth, J.R., Dollinger, G., 2015. Quantification of water in hydrous ringwoodite. *Front. Earth Sci.* 2, 38. <https://doi.org/10.3389/feart.2014.00038>.
- Thompson, A.B., 1992. Water in the Earth's upper mantle. *Nature* 358 (6384), 295. <https://doi.org/10.1038/358295a0>.
- Wang, J., Sinogeikin, S.V., Inoue, T., Bass, J.D., 2003. Elastic properties of hydrous ringwoodite. *Am. Mineral.* 88 (10), 1608–1611.
- Wang, J., Sinogeikin, S.V., Inoue, T., Bass, J.D., 2006. Elastic properties of hydrous ringwoodite at high-pressure conditions. *Geophys. Res. Lett.* 33 (14), L14308. <https://doi.org/10.1029/2006GL026441>.
- Wang, X.-C., Wilde, S.A., Li, Q.-L., Yang, Y.-N., 2015. Continental flood basalts derived from the hydrous mantle transition zone. *Nat. Commun.* 6, 7700. <https://doi.org/10.1038/ncomms8700>.